THE JOURNAL OF PHYSICAL CHEMISTRY C

Article

pubs.acs.org/JPCC

Anisotropic Lattice Thermal Conductivity and Suppressed Acoustic Phonons in MOF-74 from First Principles

Xinjiang Wang,[†] Ruiqiang Guo,[†] Dongyan Xu,[‡] JaeDong Chung,[§] Massoud Kaviany,*[,∥] and Baoling Huang*[,†]

[†]Department of Mechanical and Aerospace Engineering, The Hong Kong University of Science and Technology, Clear Water Bay, Kowloon, Hong Kong

[‡]Department of Mechanical and Automation Engineering, Chinese University of Hong Kong, Shatin, Hong Kong

[§]Department of Mechanical Engineering, Sejong University, Seoul 143-747, Republic of Korea

[∥]Department of Mechanical Engineering, University of Michigan, Ann Arbor, Michigan 48109, United States

ABSTRACT: The thermal transport properties of metal−organic frameworks (MOFs) developed for molecular storage and catalytic separations play an important role in adsorption or catalysis processes but are rarely reported. We calculate the anisotropic thermal conductivities (κ) of water-stable Zn-MOF-74 with the Boltzmann transport equation and the density-functional-based tight-binding (DFTB) method, which allows for a sufficiently large number of atoms in the simulations without much compromise on accuracy. We find an anisotropic κ of 0.44 and 0.68 W/m·K at 300 K, across and along the pore directions, with acoustic contributions of 8% and 30%, respectively. These unusually low acoustic contributions are explained by the rattling-like behavior of phonons with large vibrational amplitude, low group velocity, and large scattering rate, which are caused by the unique 1-D tubing bundle structure. On the other hand, the cylindrical pores enable larger phonon speed and higher directional structural rigidity along the pore direction, leading to a higher κ. The frequency-accumulated, directional κ is explained using the spectral analysis and correlated to the structure characteristics.

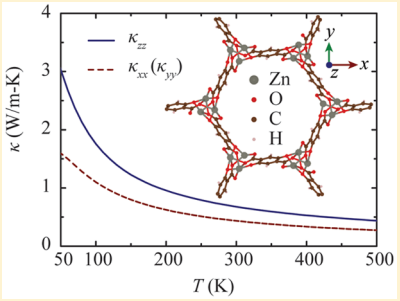

1. INTRODUCTION

Metal−organic frameworks (MOFs) usually have crystalline structures with the metal−oxygen cages linked by organic ligands. Their high adsorption surface area and tunable structures render them promising candidates for catalysis[1] and guest molecule storage and separation, including hydrogen storage,[2] carbon capture,[3] and air purification by adsorbing toxic particles.[4] However, many MOFs, such as MOF-5, are unstable against moisture, which limits their wide applications in industry. Recently, water-stable MOFs, e.g., M-MOF-74 (M = Zn, Mg, Co, and Ni), have been developed for industrial applications involving H_2O adsorption and desorption,[5−8] such as in sorption heat transformation systems.[9−13] Figure 1a,b shows the lattice structure of Zn-MOF-74, which is composed of Zn^{2+} ions and dioxidoterephthalate (DOT) linkers. The Zn−O cages are connected on one edge to construct a 1-D rod along the z axis, and six rods then form a hexagonal channel by bridging each other with DOT linkers. It is evident that this structure with $R\bar{3}$ symmetry implies anisotropy between the x−y plane and the z axis.

Although the outstanding adsorption properties of MOF-74 have been extensively studied,[3,4,14] investigations on the thermal transport properties of MOF-74 are rare; however, they play an important role in the adsorption or catalysis processes. For example, most adsorption processes are exothermic and the heat released during the adsorption could lead to the reduction in the adsorption capacity and speed[3,15] or even local overheating, which is devastative to the adsorption bed if the heat cannot be dissipated efficiently. Despite the importance of thermal properties of MOFs, there are only a few experimental results reported for crystalline MOFs due to the challenge in characterizing the thermal conductivity of small crystals. Huang et al. measured the thermal conductivity of single crystalline MOF-5 and acquired a value of 0.32 W/m·K at room temperature.[16] Liu et al. reported an effective thermal conductivity around 0.1 W/m·K for low-density MOF-5 pellets made of compressed powders,[17] close to the result from a later study.[15] Due to insufficient experimental information, it is desired to theoretically predict the lattice thermal conductivities of novel MOF structures, including MOF-74; meanwhile, the theoretical modeling will also provide insights into the mechanism of thermal transport in MOFs, which may shed light on the design of a new MOF structure with a high intrinsic thermal conductivity.

Among the few available theoretical models on the thermal properties of MOFs, the molecular dynamics (MD) simulation method is most widely used.[18−20] MD simulations conducted by Huang et al. and Zhang and Jiang reveal that the main thermal resistance in MOF-5 stems from the flexible polymeric

Received: September 5, 2015
Published: October 29, 2015

DOI: 10.1021/acs.jpcc.5b08675
J. Phys. Chem. C 2015, 119, 26000−26008

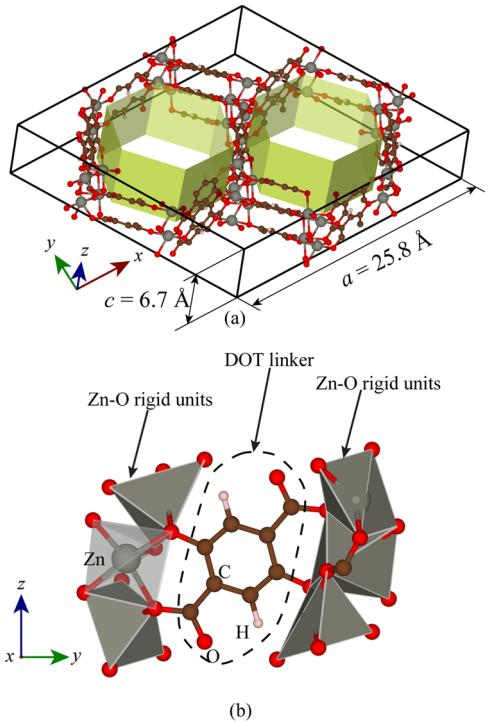

Figure 1. (a) A view of the 3-D structure of Zn-MOF-74. (b) The configuration of the Zn−O rigid units as well as the dioxidotereph-thalate (DOT) linkers.

bridges and the mass mismatch between the cages and the bridges.[18,19] Zhang and Jiang also indicated small phonon mean free paths (MFP) in ZIF-8 (zeolitic imidazolate framework-8)[18] based on information extracted from MD simulations. However, the accuracy of classical MD simulations depends on the quality of the interatomic potentials used. Although classical force fields have been successfully developed for MOF-5[21] and ZIF-8,[18] there are currently no interatomic potentials available for the MOF-74 family. Due to the complexity and variety of the structures of MOFs, it is challenging and time-consuming to develop suitable potentials for different MOF structures, and the transferability of these potentials is also a concern. Moreover, MD simulations need to sample a large amount of data and are only strictly valid when the temperature is above the Debye temperature. The analysis of the contributions of different phonon modes based on MD is not quite convenient either due to the long correlation length and simulation uncertainties involved.

Lattice dynamics (LD) calculation is another common approach in calculating thermal properties of crystalline materials. It is often combined with first-principles calculations of the harmonic and anharmonic interatomic force constants and has proved to be accurate for simple crystal systems, such as zincblendes,[22] half-Heuslers,[23] and skutterudites.[24] The combined first-principles lattice dynamics (FPLD) scheme is advantageous in transferability and accuracy, since one can yield the accurate total energy of a configuration through solving the Schrödinger equation and considering the mutual interactions among electrons and ions in various structures with different bonding configurations.[25] Moreover, the LD can yield comprehensive information for phonon transport, including phonon dispersion relation, thermal expansion, and thermal conductivity, respectively. Modewise phonon transport information, such as phonon mode lifetimes and mode contributions, can also be readily extracted. Currently, harmonic and quasi-harmonic FPLD have been applied to MOF structures.[26,27] However, using the conventional FPLD scheme to obtain thermal conductivity is still limited to simple crystals due to the computation-demanding calculation using density-functional theory (DFT). For such complex materials, with tens of atoms in one unit cell and nearly 500 atoms in an expanded supercell such as MOF-74, the conventional FPLD scheme using DFT is computationally prohibitive.

In this study, we developed a new FPLD scheme for the prediction of thermal transport properties for complex crystalline structures by combining LD calculations with the efficient and accurate density-functional-based tight-binding (DFTB)[28−32] method. Using Zn-MOF-74 as an example, we predicted the anisotropic thermal conductivity in complex MOF-74 structure with this scheme. Spectral analysis on phonon transport in MOF-74 structure was also conducted to reveal the fundamental thermal transport mechanism in the nanoporous lattice structure and to clarify the relationship between the thermal conductivity and structure.

2. THEORETICAL METHODS

2.1. Density-Functional Tight-Binding Method. The DFTB method implemented in the DFTB+ package[33] is used in this study as a substitute of DFT[34,35] to speed up the calculations without much compromise on accuracy. The DFTB method is very similar to DFT except that the Kohn−Sham total energy is expanded to the second-order in both electron and magnetization density fluctuations with the Hamiltonian matrix elements represented by linear combinations of atomic orbitals, the electron density by the Mulliken charges, and the magnetization density in terms of non-overlapping spherically symmetric functions. Detailed introduction of DFTB calculations can be found elsewhere.[28−32] With these approximations, the speed of the DFTB method has been tested to be more than 20 times faster during static calculations of MOF-74 without losing much accuracy (see later verification), making it a suitable approach for the thermal conductivity calculation for MOFs.

2.2. Harmonic Lattice Dynamics. During harmonic LD calculations, the harmonic interatomic force constants (Φ) are projected into the reciprocal space through Fourier transform and then diagonalized to acquire the eigenfrequency (ω) and eigenvector (e) of each normal vibrational mode:

$$D_{\alpha\beta}(bb',q) = \frac{1}{(m_b m_{b'})^{1/2}} \sum_{l'} \Phi_{\alpha\beta}(0b,l'b') \exp[i\mathbf{q}\cdot(\mathbf{r}(l'b') - \mathbf{r}(0b))] \quad (1)$$

$$\sum_{b'\beta} D_{\alpha\beta}(bb',q)\, e_\beta(b',\xi) = \omega^2(\xi)\, e_\alpha(b,\xi) \quad (2)$$

where the subscripts α and β denote directional components; b and l represent the atom index inside the unit cell and the cell index in the supercell, respectively. D is the dynamical matrix in the reciprocal space, and ξ represents a phonon mode identified by a wavevector $\mathbf{q}$ and polarization s.

The atomic displacement parameter is an important crystallographic parameter to represent the mean square distance of an atom under thermal vibrations. It is directly calculated in harmonic lattice dynamics with the expression[36]

DOI: 10.1021/acs.jpcc.5b08675
J. Phys. Chem. C 2015, 119, 26000−26008

$$\langle |u_\alpha(b,\xi)|^2 \rangle = \frac{\hbar}{2N_0 m_b} \frac{1+2n_\xi}{\omega(\xi)} |e_\alpha(b,\xi)|^2 \quad (3)$$

where N_0 is the number of atoms in a unit cell and n is the equilibrium phonon population obeying Bose−Einstein distribution function $n_\xi = 1/\{\exp[\hbar\omega(\xi)/k_B T] - 1\}$.

2.3. Quasi-Harmonic Lattice Dynamics. The phonon Grüneisen parameter γ is generally used for evaluating the overall anharmonic phonon scattering strength.[37,38] Under the quasi-harmonic approximation, one can acquire the phonon Grüneisen parameter without using anharmonic lattice dynamics. The modewise Grüneisen parameter is defined as $\gamma_\xi = -\mathrm{d}[\ln(\omega_\xi)]/\mathrm{d}[\ln(\Omega)]$ (Ω is the volume of the unit cell) and can be expressed through the difference method by[39]

$$\gamma_\xi = -\Delta \ln(\omega_\xi)/\Delta \ln(\Omega) \quad (4)$$

Moreover, the Grüneisen parameter can also indicate the phonon−phonon scattering strength contributed from a specific atom through the following relation[38]

$$\gamma_\alpha(\xi,b) = \gamma_\xi |e_\alpha(b,\xi)|^2 \quad (5)$$

2.4. Anharmonic Lattice Dynamics. Since MOFs without strategic treatments are poor electron conductors,[40] rendering phonons the main heat carriers, the thermal conductivity is essentially determined by the lattice conduction. The lattice thermal conductivity can be acquired by solving the Boltzmann transport equation (BTE) with the kinetic theory under the single-mode approximation when the Umklapp processes dominate the phonon transport. The lattice thermal conductivity κ can be written as[41]

$$\kappa_{\alpha\beta} = \frac{\hbar^2}{N\Omega k_B T^2} \sum_\xi v_{g,\alpha}(\xi)\, v_{g,\beta}(\xi)\, \omega^2(\xi)\, n_\xi(n_\xi+1)\tau_{pp}(\xi) \quad (6)$$

where N is the total number of q-points in the first Brillouin zone and v_g is the group velocity. τ_{pp} is the relaxation time of each phonon mode and can be acquired by counting the net scattering rate of a phonon interacting with other two phonons, i.e.,[42]

$$\frac{1}{\tau_{pp}(\xi)} = \pi \sum_{\xi',\xi''} |\varphi_3(-\xi,\xi',\xi'')|^2 \times [2(n_{\xi'} - n_{\xi''})\delta [\omega(\xi) + \omega(\xi') - \omega(\xi'')] + (1 + n_{\xi'} + n_{\xi''})\delta [\omega(\xi) - \omega(\xi') - \omega(\xi'')]] \quad (7)$$

where the summation is over all the possible phonon-scattering processes satisfying the energy conservation, which is guaranteed by the δ function, and momentum conservation, i.e., $\mathbf{q} + \mathbf{q}' \pm \mathbf{q}'' = \mathbf{g}$, where $\mathbf{g}$ is either 0 (normal) or a reciprocal lattice vector (Umklapp). $\varphi_3(\xi,\xi',\xi'')$ is the interphonon interaction strength and can be determined by

$$\varphi_3(\xi,\xi',\xi'') = \left[\frac{\hbar}{8L\omega(\xi)\,\omega(\xi')\,\omega(\xi'')}\right]^{1/2} \sum_{l'l''} \sum_{bb'b''} \sum_{\alpha\beta\gamma} \left[\Psi_{\alpha\beta\gamma}(0b,l'b',l''b'') \exp\{\mathrm{i}[\mathbf{q}\cdot\mathbf{r}(0b) + \mathbf{q}'\cdot\mathbf{r}(l'b') + \mathbf{q}''\cdot\mathbf{r}(l''b'')]\} \times \frac{e_\alpha(b|\xi)}{m_b^{1/2}} \frac{e_\beta(b'|\xi')}{m_{b'}^{1/2}} \frac{e_\gamma(b''|\xi'')}{m_{b''}^{1/2}}\right] \quad (8)$$

where L is the number of unit cells in the calculation domain and Ψ represents the real-space third-order interatomic force constants. The anharmonic lattice dynamics method is notoriously time-consuming since the summation of eq 8 is over all atoms in the supercell, making the complexity of the unit cell the bottleneck for the whole calculation process.

2.5. Calculation Procedure. In this study, both the mio-1-1[28] and Znorg-0-1[43] parameter sets were adopted for the simulation of the organic−inorganic compound MOF system using DFTB+. The relaxation over the primitive cell was conducted using a conjugate-gradient method with the Brillouin zone sampled by a 6 × 6 × 6 mesh. van der Waals corrections were also considered in DFTB+ through the Lennard-Jones dispersion model.[44] The maximum force component was set to be 10^{-6} au as the convergence standard.

The relaxed primitive unit cell containing 54 atoms was expanded to a supercell containing 486 atoms. To obtain the harmonic force constants, each independent atom was displaced by 0.01 Å while forces on all atoms in the supercell were recorded.

As for the anharmonic LD calculation, a smaller supercell containing 324 atoms was used because of the shorter interaction range of anharmonic force constants. After careful tests, an interaction cutoff distance of 8 Å was selected for the Zn, O, and C atoms while that for the H atoms was 3 Å. The delta function in eq 7 was approximated by a Gaussian function with a smearing parameter σ = 0.2 THz and a high cutoff frequency of 1.2 THz (~6σ). A 5 × 5 × 5 Monkhorst−Pack mesh scheme in the first Brillouin zone was adopted for the thermal conductivity calculation.

3. RESULTS AND DISCUSSION

3.1. Verification of DFTB Method. To testify the feasibility of DFTB, we made a comparison between DFTB and DFT with van der Waals corrections[45,46] as implemented in the Vienna Ab Initio Simulation Package (VASP).[47,48] Since the results of lattice dynamics calculation depend on the accuracy of equilibrium lattice parameters and energy drift of the minor-disturbed system, a systematic comparison between DFTB and DFT over these two properties would intuitively provide some fundamental information. In DFT calculations, the system was relaxed first with a cutoff energy of 600 eV and 3 × 3 × 3 k-point mesh in the Brillouin zone and then a supercell was created with a minimal displacement of a specific atom. The settings of dimension of the supercell and the displacement distance replicated those in the harmonic LD calculations using DFTB. Energy drifts from the equilibrium state were recorded in each minor-disturbed system and then averaged over all the disturbed supercells. Table 1 lists the parameters obtained from experiments at 300 K and the DFT and DFTB calculations for comparison, including lattice constants, volume, and average

DOI: 10.1021/acs.jpcc.5b08675
J. Phys. Chem. C 2015, 119, 26000−26008

Table 1. Zn-MOF-74 Lattice Constants, Volume, and Average Energy Difference (ΔE) in Response to a Series of Minor Displacements of All Atoms

method	a (Å)	c (Å)	volume (Å^3)	av ΔE (meV)
experiment	25.932	6.837	3981.5	
DFT	26.170	6.568	3895.7	1.706
DFTB	25.823	6.720	3880.8	1.863
difference (%)	1.33	2.31	0.38	9.20

energy difference (EDIFF) of the minor-disturbed systems. It proves that the discrepancy of the relaxed volumes using DFT and DFTB from experimental results are both small, 2.2% and 2.5%, respectively. The agreement between DFTB and DFT is even more satisfactory with only 0.4% difference. The average EDIFF calculated from DFTB is found to be within 10% error compared with the DFT result. The error is relatively small and this error mainly results in an underestimation of the high-frequency region of C−C and C−H vibrations, which contribute little to the thermal conductivity (see later phonon density of states discussions). Therefore, the DFTB is suitable for the LD calculation for such complex materials considering the balance between speed and accuracy.

3.2. Harmonic Lattice Dynamics. The phonon dispersion relation (Figure 2a) along sequential high-symmetry paths, as

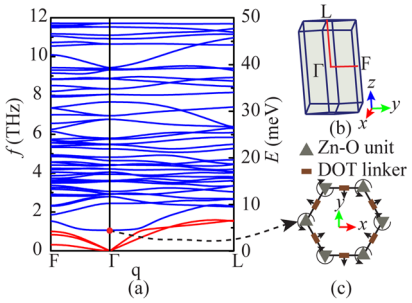

Figure 2. (a) Phonon dispersion along some high-symmetry paths. Branches with frequency above 12 THz are quite flat and thus not shown. Red and blue colors denote acoustic and optical branches, respectively. (b) High-symmetry points in the reciprocal space. (c) Sketch of the vibration states of Zn−O units and DOT linkers corresponding to the first optical mode at Γ point (dot in red in Figure 2a).

illustrated in Figure 2b, shows that the acoustic cutoff frequency is small (<2 THz). Curves above 8 THz are quite flat and thus not shown in this figure. It should be noted that the dispersion curve is anisotropic; the phonon group velocity along the Γ−L (z axis) direction is generally higher than that along the Γ−F (y axis) direction. According to eq 6, a larger phonon group velocity is expected to result in a higher thermal conductivity. Here the first optical branch (O1), an important contributor to the anisotropy of the thermal conductivity (see section 3.4), is analyzed in terms of the corresponding vibrational eigenstates of all atoms, as an example to demonstrate the anisotropy of the material. As shown in Figure 2c, the first optical branch corresponds to the rotation of quasi-1-D chains composed of Zn−O units and the flapping behavior of DOT linkers. Then the larger group velocity along the pore direction of the first optical phonon branch can be explained by the faster transport of twisting behaviors along the quasi-1-D chains than that in the x−y plane because of the soft DOT linkers in the x−y plane. Therefore, the tubelike structure and the DOT linkers connecting neighboring Zn−O chains provide the structural explanation of the anisotropic phonon transport behavior of MOF-74.

It should be noted that the lowest acoustic branch (TA1) along the Γ−F direction (along the y axis) is very soft and has a projected group velocity 515 m/s near the Γ point, which is much lower than the values of the other two acoustic branches (3258 and 3656 m/s). Further analysis on the eigenmodes of the phonon branch indicates that the transverse vibrational mode among the hexagonal pores features the ultrasoft branch, which can be also proved by further calculations of the elastic constants. The calculated shear modulus in the x-y plane is c_{66} = 2.1 GPa, much lower than c_{11} (16.9 GPa), c_{33} (26.9 GPa), and also another shear modulus c_{44} (15.4 GPa). For the same reason, the large pores inside the MOF-74 structure are likely to collapse under high shear strain, which is also a feature of other MOFs with large porosity ratio.[26]

Moreover, the group velocity of the low-frequency optical phonons (especially for the off-center q-points) is comparable to that of acoustic phonons, indicating that the thermal conductivity from these branches is non-negligible. The phonon dispersion relation also implies a large scattering rate (i.e., a small relaxation time) due to the dense and intertwined bands, potentially leading to a low thermal conductivity.

The density of states associated with each species [$D(f)$, such that $\int D(f)\,df = 3N_s$, where N_s is the total number of atoms] along with the total are shown in Figure 3. Both the $D(f)$

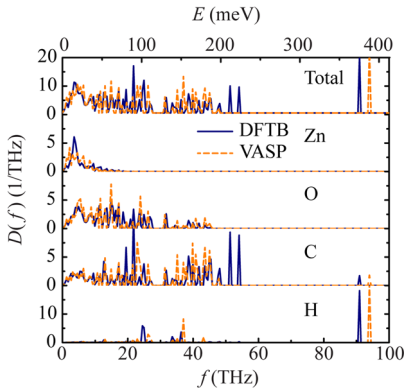

Figure 3. Total phonon density of states and that coming from each species of atoms.

calculated using DFTB and DFT are shown and they generally coincide despite an underestimation of frequency for the high-frequency phonons by DFTB. The discrepancies at around 54 and 91 THz derive from DFTB prediction of a weaker interaction strength between C−C and C−H, respectively, as seen from the comparison of $D(f)$ of C and H atoms. However, since the frequencies of these modes are very high and the phonon dispersion curves are fairly flat, the populations and group velocities of these phonons are negligible, thus contributing little to the thermal conductivity. Therefore, the general prediction of the $D(f)$ from DFTB calculations can be used without much compromise on accuracy.

It should also be noted that both calculations predict that even though the total $D(f)$ has a wide frequency range, up to over 90 THz, the $D(f)$ of the Zn atoms is nearly 0 above 20 THz, which implies a significant density of states mismatch between Zn and other atoms. Since the Zn atoms serve as the

DOI: 10.1021/acs.jpcc.5b08675
J. Phys. Chem. C 2015, 119, 26000−26008

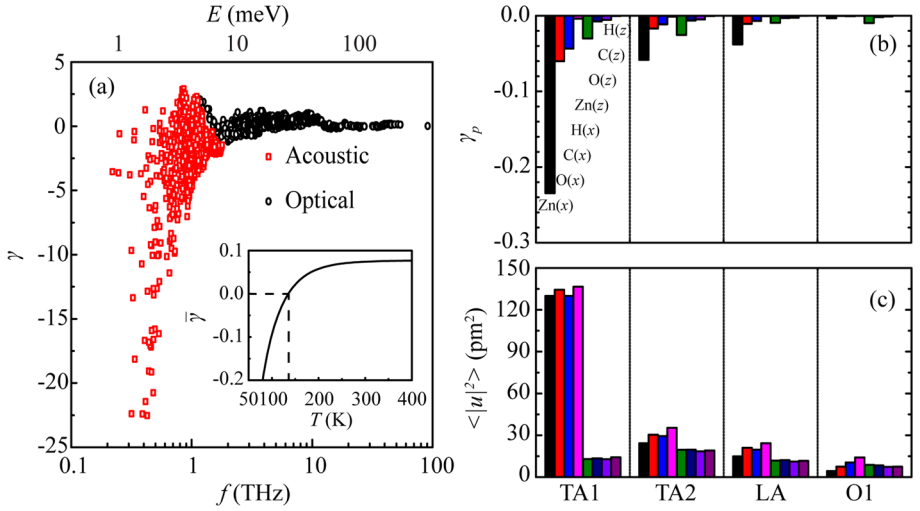

Figure 4. (a) Variations of the spectral, mode-dependent Grüneisen parameter (γ) with respect to frequency. (b) Projected Grüneisen parameter (γ_p) for each species along the x and z directions. (c) Spectral atomic displacement parameter ($\langle|u|^2\rangle$, also known as ADP) for each species at 300 K along the x and z directions. Only the lowest four phonon branches are shown with the acronyms TA1 (first transverse acoustic mode), TA2 (second transverse acoustic mode), LA (longitudinal acoustic mode), and O1 (first optical mode).

backbones for phonons to transport in all directions (Figure 1), this density of states mismatch affects all directions, which diminishes contributions of phonons with frequency above 20 THz as heat carriers. The density of states mismatch would also result in relatively small thermal conductivity.[49]

3.3. Quasi-Harmonic Lattice Dynamics. Using the quasi-harmonic method introduced in section 2.3, the phonon Grüneisen parameters (γ) were calculated and are shown in Figure 4a,b. The phonons with low frequencies, especially acoustic phonons, have large negative Grüneisen values. The negative Grüneisen parameters are caused by the flapping and wiggling behavior of the benzene rings[27] and may result in a negative thermal expansion coefficient of MOF-74 at low temperatures,[50] which is displayed in the inset of Figure 4a. The negative heat-capacity-averaged Grüneisen parameter ($\bar{\gamma}$) at low temperatures implies a negative thermal expansion due to the positive correlation relation between these two parameters.[39] Unlike other MOFs that have been reported with a negative thermal expansion even at the room temperature,[27] MOF-74 experiences a transition from negative thermal expansion to positive at around 140 K.

Moreover, the large absolute values of the Grüneisen parameter of the acoustic phonons provide a direct insight into the strong anharmonicity of the crystal with even low-frequency vibrations,[51,52] since the phonon scattering rate (Γ) is generally considered as $\Gamma \propto |\gamma|^2$. This phenomenon is elaborated in Figure 4b by projecting the Grüneisen parameter of the lowest four phonon branches onto each individual atom and axis using eq 5. First, it is noted that the projected Grüneisen parameter (γ_p) of Zn atoms, along either x axis or z axis, has a much larger absolute value than that of the other atoms. It indicates that the Zn atoms act as the scattering center for the phonon transport, possibly due to the strong anharmonic Zn−O bonds. Moreover, the γ_p of the TA1 (first transverse acoustic) phonon branch stands out for its unmatched large absolute value compared with other phonon branches. One can also find that, especially for Zn atoms, the $|\gamma_p|$ along the x axis is much larger than that along the z axis, indicating a comparably larger scattering strength in the cross-pore plane. The atomic displacement parameter at 300 K in Figure 4c may provide insights into the mentioned unusual Grüneisen parameter behaviors. The atomic displacement parameter ($\langle|u|^2\rangle$, i.e., ADP) was calculated using eq 3. It is found that the ADP of the acoustic phonons along the x axis are significantly larger than those along z. Especially the ADP of TA1 phonons for each atom reaches as high as 130 pm^2, an amplitude high enough to feature a rattling-like behavior of all the atoms.[53] The rather high ADP is due to the quite small shear modulus in the x−y plane (c_{66}) as described in section 3.2. Since the farther an atom moves away from its equilibrium position, the more anharmonicity arises, the larger atomic displacement along the x axis would result in stronger anharmonic scatterings for the phonon transport in this direction. Therefore, the rattling-like behavior of acoustic phonons is responsible for the large absolute value of the Grüneisen parameter of acoustic phonons.

3.4. Thermal Conductivity. After obtaining the anharmonic interatomic force constants, one can calculate the lattice thermal conductivity κ through eqs 6−8. The calculated temperature-dependent thermal conductivity is shown in Figure 5a,b. The thermal conductivity tensor is anisotropic: κ_{zz} = 0.68 and κ_{xx} = κ_{yy} = 0.44 W/m·K at room temperature. The exact solution of BTE is also acquired through the iterative method;[54] however, the differences are within 2% for both κ_{zz} and κ_{xx}. Therefore, the results from the single-mode relaxation time model are retained in the discussions due to its explicit inclusion of the phonon relaxation times. Overall, the calculated thermal conductivity along the pore is around 30% higher than that in the x−y plane, as a result of the slightly higher group velocity along the pore, as discussed in section 3.2. It should also be noted that the thermal conductivity decreases as temperature increases. Moreover, a linear relationship between κ and $1/T$ for both κ_{xx} and κ_{zz} is observed above 100 K, a typical behavior for single crystals.[23,24,55] Together shown in Figure 5a,b is the mode contribution to thermal conductivity from acoustic and optical phonons. The acoustic phonons contribute only 30% to κ_{zz} at 300 K while the fraction is even smaller (8% at 300 K) for κ_{xx}. In this rendering of the thermal conductivity contribution, the acoustic phonons are largely overshadowed by the optical phonons. On the one hand,

DOI: 10.1021/acs.jpcc.5b08675
J. Phys. Chem. C 2015, 119, 26000−26008

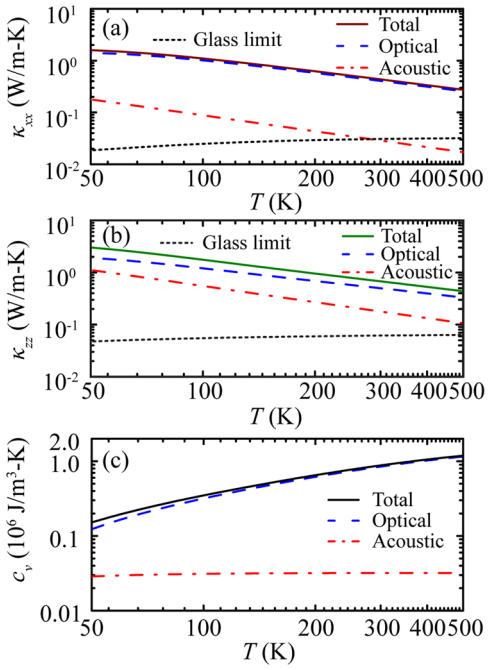

Figure 5. (a) Temperature dependence of κ_{xx}. (b) Temperature dependence of κ_{zz}. (c) Temperature-dependent heat capacity of MOF-74. The glass limit of thermal conductivity is calculated using the amorphous limit in which $\tau_{pp} = 1/(2f)$, as proposed by Cahill et al.[56,57]

due to the complex unit cell of the crystal, the $D(f)$ of the optical phonons dominates over the acoustic phonons, which can be seen from the small acoustic cutoff frequency in Figure 2a. On the other hand, the relatively large group velocity of low-frequency optical phonons (discussed above) helps the transport of optical phonons, making them the major heat carriers. The glass limit is calculated using an extreme case for the relaxation time proposed by Cahill et al.[56,57] in which the relaxation time of a phonon is limited by half its vibrational period; i.e., $\tau = 1/(2f)$. Therefore, the relaxation time is independent of the temperature in this case and the predicted thermal conductivity increases with temperature as a result of increasing heat capacity, as seen in Figure 5c. From 50 to 500 K, the total thermal conductivity calculated from DFTB decreases with temperature, while the trend is the opposite for the Cahill amorphous model. As expected, the total thermal conductivity values of Zn-MOF-74 in both directions are larger than the glass limit in the temperature range.

Figure 6a plots the cumulative contribution to thermal conductivity in terms of phonon frequencies. It is observed that the cumulative contribution almost saturates for both κ_{xx} and κ_{zz} at 20 THz, confirming that the phonons with a frequency above 20 THz contribute little to the thermal conductivity of Zn-MOF-74 due to the vibrational density of states mismatch between the Zn and other atoms. In order to further illustrate the anisotropy of MOF-74, we compare the frequency contribution to κ_{zz} and κ_{xx} and find that κ_{zz} increases much more than κ_{xx} from 0.9 to 2 THz and then becomes parallel after 2 THz. This indicates that the origin of different values of κ_{zz} and κ_{xx} lies mainly on phonons of frequency from 0.9 to 2 THz. The frequency-dependent group velocity is shown in Figure 6b. The group velocity in x and z directions mainly differs from 0.1 to 2 THz. But since the values of the phonon density of states below 0.9 THz are quite small, the thermal conductivity contribution from these phonons is low for both

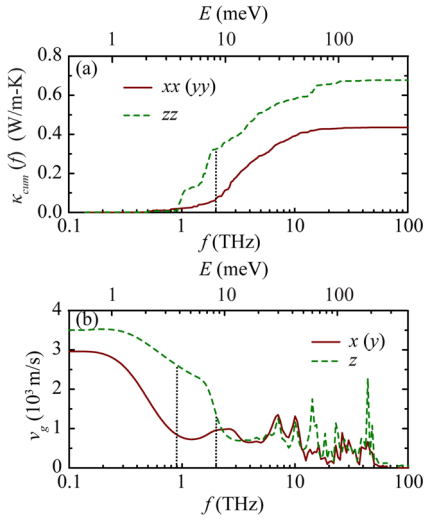

Figure 6. (a) Cumulative thermal conductivity (κ_{xx} and κ_{zz}) with respect to frequency at 300 K [$\kappa_{cum}(f) = \int_0^f \kappa(f')\,df'$] and (b) phonon group velocity as a function of frequency along both x (y) and z directions.

κ_{zz} and κ_{xx}, causing negligible difference between them. Therefore, the main contributors to the anisotropic thermal conductivity are phonons from 0.9 to 2 THz, overlapping with the range of the higher two acoustic branches and the first optical branch, as seen in Figure 2a.

However, the DOS and group velocity cannot totally explain the thermal conductivity. One needs to explore the details of anharmonic phonon scatterings as well to unveil the origin of the thermal conductivity and the large contribution from optical phonons. Figure 7 plots the cumulative contribution to

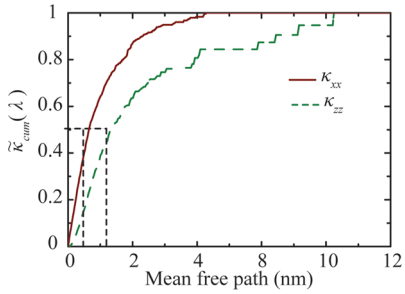

Figure 7. Normalized cumulative thermal conductivity at 300 K as a function of the mean free path (λ), $\tilde{\kappa}_{cum}(\lambda) = \int_0^\lambda \kappa(\lambda')\,d\lambda' / \int_0^\infty \kappa(\lambda')\,d\lambda'$.

thermal conductivity with respect to the phonon mean free path (λ, MFP) at 300 K. It is seen that phonons with $\lambda < 2$ nm contribute more than 50% to both κ_{zz} and κ_{xx} while those with λ larger than 10 nm contribute little. The 50% contribution λ of MOF-74 is indeed very low for such a crystalline structure, compared with the value of around 300 nm in Si.[58] This suggests that the thermal transport in Zn-MOF-74 is dominated by the short-MFP phonons, indicating that strong anharmonic phonon scatterings in Zn-MOF-74 quickly damp the lattice vibrations and block the transport of phonons. It can also be noted that the phonon mean free path along the z direction is roughly twice that along the x axis, mainly due to the higher anisotropic group velocity in the z direction. The large scattering rate can also be observed in the plot of

DOI: 10.1021/acs.jpcc.5b08675
J. Phys. Chem. C 2015, 119, 26000−26008

relaxation time with regard to the frequency shown in Figure 8. The majority of phonons have a relaxation time between 0.3

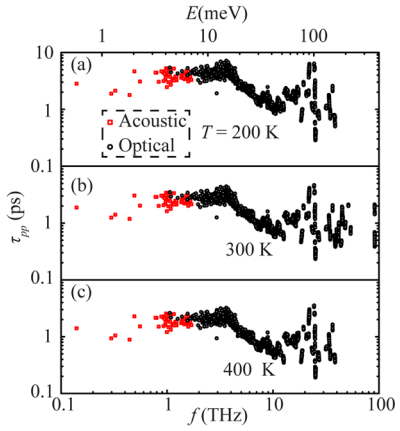

Figure 8. Frequency-dependent phonon−phonon interaction time (τ_{pp}) at (a) 200 K, (b) 300 K, and (c) 400 K, with distinction between acoustic and optical phonons.

and 5 ps at 300 K. This is a small range for the relaxation time of a crystalline structure, which would span 2−3 orders of magnitude in simple crystals such as Si,[22] Lennard-Jones argon crystal,[59] and PbTe.[60] Through the dependence of the relaxation time on temperature from 200 to 400 K shown in Figure 8a−c, it can be observed clearly that the relaxation time decreases with temperature. This phenomenon explains the decreasing behavior of the thermal conductivity with the temperature, even though the heat capacity increases. Another phenomenon is the unusual behavior of relaxation time when the frequency approaches zero. Unlike other crystals, for which a $\tau_{pp} \sim \omega^{-2}$ or $\tau_{pp} \sim \omega^{-3}$ trend is usually observed,[22,60] the relaxation time values of acoustic phonons of Zn-MOF-74 are more likely to be slightly increasing instead of decreasing with the increase in frequency. Such a phenomenon implies superstrong anharmonicity of acoustic phonons, which is due to the rattling-like behavior[38] of acoustic phonons, especially the TA1 phonons, as depicted in Figure 4c. For this reason, some acoustic phonon modes in Zn-MOF-74 at high temperatures are close to the situation where phonons are "equally strongly damped" as in amorphous phase, as described by Cahill and Pohl.[56] On the one hand, the thermal conductivity decreases with the temperature, a typical trend for crystalline structures. On the other hand, due to the complex structure and large porosity ratio, scatterings are strong for all phonons at high temperatures,[61,62] which would eventually result in blocking phonons from propagating, as in phonon-glass materials.[56]

4. CONCLUSIONS

We have calculated the lattice thermal conductivity of Zn-MOF-74 (crystalline but with a large and complex unit cell) at different temperatures using DFTB together with the lattice dynamics approach. The calculated thermal conductivity is anisotropic (0.44 W/m·K in the cross-pore plane and 0.68 W/m·K along the pore direction). The optical phonons account the most for the thermal conductivity contribution at room temperature due to their (i) dominating density of states, (ii) relatively large group velocity, and (iii) comparable relaxation time with acoustic phonons. It is found that the Zn atoms experience the highest anharmonicity in their acoustic vibrations and that the small shear modulus in the cross-pore plane prohibits a larger contribution of the acoustic phonons to the thermal conductivity due to the low group velocity and high vibration amplitude (large anharmonicity) of the acoustic phonons. Therefore, modifications strengthening the structure have the potential to increase the thermal conductivity of MOF-74. For example, substitution of the Zn atoms can increase the tensile strength, or selective adsorption on the DOT linkers can change the shear modulus of MOF-74, allowing one to tune the thermal conductivity. It is also found that while the thermal conductivity decreases with temperature, as in other crystals (at high temperatures), some acoustic phonons suffer superstrong anharmonic scattering, as in the phonon-glass solids, due to their rattling-like behavior.

AUTHOR INFORMATION

Corresponding Authors

*M.K. e-mail: kaviany@umich.edu.

*B.H. e-mail: mebhuang@ust.hk.

Notes

The authors declare no competing financial interest.

ACKNOWLEDGMENTS

B.H. is thankful for the financial support from the Hong Kong General Research Fund (Grant Nos. 613413 and 623212). J.D.C. and M.K. are thankful for support by Energy Efficiency & Resources (Award No. 20122010100120) of Korea Institute of Energy Technology Evaluation and Planning funded by Ministry of Knowledge Economy.

REFERENCES

(1) Llabrés i Xamena, F. X.; Abad, A.; Corma, A.; Garcia, H. MOFs as Catalysts: Activity, Reusability and Shape-Selectivity of a Pd-Containing MOF. *J. Catal.* **2007**, *250* (2), 294−298.

(2) Rosi, N. L.; Eckert, J.; Eddaoudi, M.; Vodak, D. T.; Kim, J.; O'Keeffe, M.; Yaghi, O. M. Hydrogen Storage in Microporous Metal-Organic Frameworks. *Science* **2003**, *300* (5622), 1127−1129.

(3) Valenzano, L.; Civalleri, B.; Chavan, S.; Palomino, G. T.; Areán, C. O.; Bordiga, S. Computational and Experimental Studies on the Adsorption of CO, N_2, and CO_2 on Mg-MOF-74. *J. Phys. Chem. C* **2010**, *114* (25), 11185−11191.

(4) Grant Glover, T.; Peterson, G. W.; Schindler, B. J.; Britt, D.; Yaghi, O. MOF-74 Building Unit Has a Direct Impact on Toxic Gas Adsorption. *Chem. Eng. Sci.* **2011**, *66* (2), 163−170.

(5) Low, J. J.; Benin, A. I.; Jakubczak, P.; Abrahamian, J. F.; Faheem, S. A.; Willis, R. R. Virtual High Throughput Screening Confirmed Experimentally: Porous Coordination Polymer Hydration. *J. Am. Chem. Soc.* **2009**, *131* (43), 15834−15842.

(6) Cychosz, K. A.; Matzger, A. J. Water Stability of Microporous Coordination Polymers and the Adsorption of Pharmaceuticals from Water. *Langmuir* **2010**, *26* (22), 17198−17202.

(7) Saha, D.; Deng, S. Structural Stability of Metal Organic Framework MOF-177. *J. Phys. Chem. Lett.* **2010**, *1* (1), 73−78.

(8) Greathouse, J. A.; Allendorf, M. D. The Interaction of Water with MOF-5 Simulated by Molecular Dynamics. *J. Am. Chem. Soc.* **2006**, *128* (33), 10678−10679.

(9) Tan, K.; Zuluaga, S.; Gong, Q.; Canepa, P.; Wang, H.; Li, J.; Chabal, Y. J.; Thonhauser, T. Water Reaction Mechanism in Metal Organic Frameworks with Coordinatively Unsaturated Metal Ions: MOF-74. *Chem. Mater.* **2014**, *26* (23), 6886−6895.

(10) Jänchen, J.; Ackermann, D.; Stach, H.; Brösicke, W. Studies of the Water Adsorption on Zeolites and Modified Mesoporous Materials for Seasonal Storage of Solar Heat. *Sol. Energy* **2004**, *76* (1), 339−344.

DOI: 10.1021/acs.jpcc.5b08675
J. Phys. Chem. C 2015, 119, 26000−26008

(11) Henninger, S. K.; Schmidt, F. P.; Henning, H.-M. Water Adsorption Characteristics of Novel Materials for Heat Transformation Applications. *Appl. Therm. Eng.* **2010**, *30* (13), 1692−1702.
(12) Ehrenmann, J.; Henninger, S. K.; Janiak, C. Water Adsorption Characteristics of MIL-101 for Heat-Transformation Applications of MOFs. *Eur. J. Inorg. Chem.* **2011**, *2011* (4), 471−474.
(13) Jeremias, F.; Fröhlich, D.; Janiak, C.; Henninger, S. K. Water and Methanol Adsorption on MOFs for Cycling Heat Transformation Processes. *New J. Chem.* **2014**, *38* (5), 1846−1852.
(14) Li, Y.; Wang, X.; Xu, D.; Chung, J. D.; Kaviany, M.; Huang, B. H_2O Adsorption/Desorption in MOF-74: Ab Initio Molecular Dynamics and Experiments. *J. Phys. Chem. C* **2015**, *119* (23), 13021−13031.
(15) Ming, Y.; Purewal, J.; Liu, D.; Sudik, A.; Xu, C.; Yang, J.; Veenstra, M.; Rhodes, K.; Soltis, R.; Warner, J.; et al. Thermophysical Properties of MOF-5 Powders. *Microporous Mesoporous Mater.* **2014**, *185*, 235−244.
(16) Huang, B. L.; Ni, Z.; Millward, A.; McGaughey, A. J. H.; Uher, C.; Kaviany, M.; Yaghi, O. Thermal Conductivity of a Metal-Organic Framework (MOF-5): Part II. Measurement. *Int. J. Heat Mass Transfer* **2007**, *50* (3−4), 405−411.
(17) Liu, D.; Purewal, J. J.; Yang, J.; Sudik, A.; Maurer, S.; Mueller, U.; Ni, J.; Siegel, D. J. MOF-5 Composites Exhibiting Improved Thermal Conductivity. *Int. J. Hydrogen Energy* **2012**, *37* (7), 6109−6117.
(18) Zhang, X.; Jiang, J. Thermal Conductivity of Zeolitic Imidazolate Framework-8: A Molecular Simulation Study. *J. Phys. Chem. C* **2013**, *117* (36), 18441−18447.
(19) Huang, B. L.; McGaughey, A. J. H.; Kaviany, M. Thermal Conductivity of Metal-Organic Framework 5 (MOF-5): Part I. Molecular Dynamics Simulations. *Int. J. Heat Mass Transfer* **2007**, *50* (3−4), 393−404.
(20) Han, L.; Budge, M.; Alex Greaney, P. Relationship between Thermal Conductivity and Framework Architecture in MOF-5. *Comput. Mater. Sci.* **2014**, *94*, 292−297.
(21) Greathouse, J. A.; Allendorf, M. D. Force Field Validation for Molecular Dynamics Simulations of IRMOF-1 and Other Isoreticular Zinc Carboxylate Coordination Polymers. *J. Phys. Chem. C* **2008**, *112* (15), 5795−5802.
(22) Esfarjani, K.; Chen, G.; Stokes, H. T. Heat Transport in Silicon from First-Principles Calculations. *Phys. Rev. B: Condens. Matter Mater. Phys.* **2011**, *84* (8), 085204.
(23) Shiomi, J.; Esfarjani, K.; Chen, G. Thermal Conductivity of Half-Heusler Compounds from First-Principles Calculations. *Phys. Rev. B: Condens. Matter Mater. Phys.* **2011**, *84* (10), 104302.
(24) Guo, R.; Wang, X.; Huang, B. Thermal Conductivity of Skutterudite $CoSb_3$ from First Principles: Substitution and Nanoengineering Effects. *Sci. Rep.* **2015**, *5*, 7806.
(25) Payne, M. C.; Teter, M. P.; Allan, D. C.; Arias, T. A.; Joannopoulos, J. D. Iterative Minimization Techniques for Ab Initio Total-Energy Calculations: Molecular Dynamics and Conjugate Gradients. *Rev. Mod. Phys.* **1992**, *64* (4), 1045−1097.
(26) Zhou, W.; Yildirim, T. Lattice Dynamics of Metal-Organic Frameworks: Neutron Inelastic Scattering and First-Principles Calculations. *Phys. Rev. B: Condens. Matter Mater. Phys.* **2006**, *74* (18), 180301.
(27) Zhou, W.; Wu, H.; Yildirim, T.; Simpson, J. R.; Walker, A. R. H. Origin of the Exceptional Negative Thermal Expansion in Metal-Organic Framework-5 Zn_4O(1,4-benzenedicarboxylate)$_3$. *Phys. Rev. B: Condens. Matter Mater. Phys.* **2008**, *78* (5), 054114.
(28) Elstner, M.; Porezag, D.; Jungnickel, G.; Elsner, J.; Haugk, M.; Frauenheim, T.; Suhai, S.; Seifert, G. Self-Consistent-Charge Density-Functional Tight-Binding Method for Simulations of Complex Materials Properties. *Phys. Rev. B: Condens. Matter Mater. Phys.* **1998**, *58* (11), 7260−7268.
(29) Elstner, M.; Frauenheim, T.; Kaxiras, E.; Seifert, G.; Suhai, S. A Self-Consistent Charge Density-Functional Based Tight-Binding Scheme for Large Biomolecules. *Phys. Status Solidi B* **2000**, *217* (1), 357−376.
(30) Frauenheim, T.; Seifert, G.; Elsterner, M.; Hajnal, Z.; Jungnickel, G.; Porezag, D.; Suhai, S.; Scholz, R. A Self-Consistent Charge Density-Functional Based Tight-Binding Method for Predictive Materials Simulations in Physics, Chemistry and Biology. *Phys. Status Solidi B* **2000**, *217* (1), 41−62.
(31) Frauenheim, T.; Seifert, G.; Elstner, M.; Niehaus, T.; Köhler, C.; Amkreutz, M.; Sternberg, M.; Hajnal, Z.; Carlo, A. D.; Suhai, S. Atomistic Simulations of Complex Materials: Ground-State and Excited-State Properties. *J. Phys.: Condens. Matter* **2002**, *14* (11), 3015.
(32) Elstner, M.; Frauenheim, T.; Suhai, S. An Approximate DFT Method for QM/MM Simulations of Biological Structures and Processes. *J. Mol. Struct.: THEOCHEM* **2003**, *632* (1−3), 29−41.
(33) Aradi, B.; Hourahine, B.; Frauenheim, T. DFTB+, a Sparse Matrix-Based Implementation of the DFTB Method. *J. Phys. Chem. A* **2007**, *111* (26), 5678−5684.
(34) Hohenberg, P.; Kohn, W. Inhomogeneous Electron Gas. *Phys. Rev.* **1964**, *136* (3B), B864−B871.
(35) Kohn, W.; Sham, L. J. Self-Consistent Equations Including Exchange and Correlation Effects. *Phys. Rev.* **1965**, *140* (4A), A1133−A1138.
(36) Dove, M. T. How Far Do the Atoms Move? In *Introduction to Lattice Dynamics*; Cambridge University Press: New York, 1993; pp 55−62.
(37) Nika, D. L.; Pokatilov, E. P.; Askerov, A. S.; Balandin, A. A. Phonon Thermal Conduction in Graphene: Role of Umklapp and Edge Roughness Scattering. *Phys. Rev. B: Condens. Matter Mater. Phys.* **2009**, *79* (15), 155413.
(38) Qiu, W.; Xi, L.; Wei, P.; Ke, X.; Yang, J.; Zhang, W. Part-Crystalline Part-Liquid State and Rattling-like Thermal Damping in Materials with Chemical-Bond Hierarchy. *Proc. Natl. Acad. Sci. U. S. A.* **2014**, *111* (42), 15031−15035.
(39) Srivastava, G. P. The Quasi-Harmonic Approximation. In *The Physics of Phonons*; CRC Press: Boca Raton, FL, 1990; pp 115−119.
(40) Talin, A. A.; Centrone, A.; Ford, A. C.; Foster, M. E.; Stavila, V.; Haney, P.; Kinney, R. A.; Szalai, V.; El Gabaly, F.; Yoon, H. P.; et al. Tunable Electrical Conductivity in Metal-Organic Framework Thin-Film Devices. *Science* **2014**, *343* (6166), 66−69.
(41) Broido, D. A.; Malorny, M.; Birner, G.; Mingo, N.; Stewart, D. A. Intrinsic Lattice Thermal Conductivity of Semiconductors from First Principles. *Appl. Phys. Lett.* **2007**, *91* (23), 231922.
(42) Chaput, L.; Togo, A.; Tanaka, I.; Hug, G. Phonon-Phonon Interactions in Transition Metals. *Phys. Rev. B: Condens. Matter Mater. Phys.* **2011**, *84* (9), 094302.
(43) Moreira, N. H.; Dolgonos, G.; Aradi, B.; da Rosa, A. L.; Frauenheim, T. Toward an Accurate Density-Functional Tight-Binding Description of Zinc-Containing Compounds. *J. Chem. Theory Comput.* **2009**, *5* (3), 605−614.
(44) Zhechkov, L.; Heine, T.; Patchkovskii, S.; Seifert, G.; Duarte, H. A. An Efficient *a Posteriori* Treatment for Dispersion Interaction in Density-Functional-Based Tight Binding. *J. Chem. Theory Comput.* **2005**, *1* (5), 841−847.
(45) Klimeš, J.; Bowler, D. R.; Michaelides, A. Chemical Accuracy for the van Der Waals Density Functional. *J. Phys.: Condens. Matter* **2010**, *22* (2), 022201.
(46) Klimeš, J.; Bowler, D. R.; Michaelides, A. Van Der Waals Density Functionals Applied to Solids. *Phys. Rev. B: Condens. Matter Mater. Phys.* **2011**, *83* (19), 195131.
(47) Kresse, G.; Furthmüller, J. Efficient Iterative Schemes for Ab Initio Total-Energy Calculations Using a Plane-Wave Basis Set. *Phys. Rev. B: Condens. Matter Mater. Phys.* **1996**, *54* (16), 11169−11186.
(48) Kresse, G.; Furthmüller, J. Efficiency of Ab-Initio Total Energy Calculations for Metals and Semiconductors Using a Plane-Wave Basis Set. *Comput. Mater. Sci.* **1996**, *6* (1), 15−50.
(49) Guo, R.; Huang, B. Thermal Transport in Nanoporous Si: Anisotropy and Junction Effects. *Int. J. Heat Mass Transfer* **2014**, *77*, 131−139.
(50) Gupta, M. K.; Mittal, R.; Chaplot, S. L. Negative Thermal Expansion in Cubic ZrW_2O_8: Role of Phonons in the Entire Brillouin

DOI: 10.1021/acs.jpcc.5b08675
J. Phys. Chem. C 2015, 119, 26000−26008

Zone from *ab Initio* Calculations. *Phys. Rev. B: Condens. Matter Mater. Phys.* **2013**, *88* (1), 014303.
(51) Morelli, D. T.; Heremans, J. P.; Slack, G. A. Estimation of the Isotope Effect on the Lattice Thermal Conductivity of Group IV and Group III-V Semiconductors. *Phys. Rev. B: Condens. Matter Mater. Phys.* **2002**, *66* (19), 195304.
(52) Slack, G. A.; Oliver, D. W.; Horn, F. H. Thermal Conductivity of Boron and Some Boron Compounds. *Phys. Rev. B* **1971**, *4* (6), 1714−1720.
(53) Sales, B. C.; Mandrus, D.; Chakoumakos, B. C.; Keppens, V.; Thompson, J. R. Filled Skutterudite Antimonides: Electron Crystals and Phonon Glasses. *Phys. Rev. B: Condens. Matter Mater. Phys.* **1997**, *56* (23), 15081.
(54) Fugallo, G.; Lazzeri, M.; Paulatto, L.; Mauri, F. Ab Initio Variational Approach for Evaluating Lattice Thermal Conductivity. *Phys. Rev. B: Condens. Matter Mater. Phys.* **2013**, *88* (4), 045430.
(55) Pisoni, A.; Jaćimović, J.; Barišić, O. S.; Spina, M.; Gaál, R.; Forró, L.; Horváth, E. Ultra-Low Thermal Conductivity in Organic−Inorganic Hybrid Perovskite $CH_3NH_3PbI_3$. *J. Phys. Chem. Lett.* **2014**, *5*, 2488−2492.
(56) Cahill, D. G.; Pohl, R. O. Lattice Vibrations and Heat Transport in Crystals and Glasses. *Annu. Rev. Phys. Chem.* **1988**, *39* (1), 93−121.
(57) Cahill, D. G.; Watson, S. K.; Pohl, R. O. Lower Limit to the Thermal Conductivity of Disordered Crystals. *Phys. Rev. B: Condens. Matter Mater. Phys.* **1992**, *46* (10), 6131−6140.
(58) Wang, X.; Huang, B. Computational Study of In-Plane Phonon Transport in Si Thin Films. *Sci. Rep.* **2014**, *4*, 6399.
(59) McGaughey, A. J. H.; Kaviany, M. Quantitative Validation of the Boltzmann Transport Equation Phonon Thermal Conductivity Model under the Single-Mode Relaxation Time Approximation. *Phys. Rev. B: Condens. Matter Mater. Phys.* **2004**, *69* (9), 094303.
(60) Tian, Z.; Garg, J.; Esfarjani, K.; Shiga, T.; Shiomi, J.; Chen, G. Phonon Conduction in PbSe, PbTe, and $PbTe_{1-x}Se_x$ from First-Principles Calculations. *Phys. Rev. B: Condens. Matter Mater. Phys.* **2012**, *85* (18), 184303.
(61) Chung, J. D.; Kaviany, M. Effects of Phonon Pore Scattering and Pore Randomness on Effective Conductivity of Porous Silicon. *Int. J. Heat Mass Transfer* **2000**, *43* (4), 521−538.
(62) Lindsay, L.; Li, W.; Carrete, J.; Mingo, N.; Broido, D. A.; Reinecke, T. L. Phonon Thermal Transport in Strained and Unstrained Graphene from First Principles. *Phys. Rev. B: Condens. Matter Mater. Phys.* **2014**, *89* (15), 155426.

DOI: 10.1021/acs.jpcc.5b08675
J. Phys. Chem. C 2015, 119, 26000−26008